Reversed Structure Based PI-Lead Controller Antiwindup Design and Self-Commissioning Strategy for Servo Drive Systems

Chen, Yangyang; Yang, Ming; Liu, Kaiyuan; Long, Jiang; Xu, Dianguo; Blaabjerg, Frede

Published in:
I E E E Transactions on Industrial Electronics

DOI (link to publication from Publisher):
10.1109/TIE.2021.3097602

Publication date:
2022

Document Version
Accepted author manuscript, peer reviewed version

Reversed-Structure-Based PI-Lead Controller Anti-Windup Design and Self-Commissioning Strategy for Servo Drive Systems

Yangyang Chen, *Student Member, IEEE,* Ming Yang, *Senior Member, IEEE,* Kaiyuan Liu, Jiang Long, Dianguo Xu, *Fellow, IEEE,* Frede Blaabjerg, *Fellow, IEEE*

***Abstract*- Nowadays, the dual closed-loop Proportional-Integral-Lead (PI-Lead) controller is widely used, especially for the servo systems where high performance is required for motion control, like lithography machines and vehicle-used Lidars. Considering complex industrial applications and working conditions, more comprehensive and systematic research about the structure and potential problem of the PI-Lead controller is necessary for enhancing its performance and robustness. In this paper, the failure mechanism of the classic Anti-Windup methods in the PI-Lead controller is analyzed. By adjusting the location of control blocks, a novel reversed-structure-based PI-Lead controller is proposed as a complement to the traditional anti-windup methods for effective operation and to make the system stable under severe impact disturbances. Then, a self-commissioning strategy is designed, based on a Fast Root Mean Square Error (FRMSE) index and without additional manual tuning factors. Compared with classic indicators, the proposed FRMSE index can achieve faster instability detection and accelerate the tuning process to protect the equipment.[1]**

***Index Terms*—Anti-windup, PI-Lead controller, Self-commissioning.**

NOMENCLATURE

J_m, J inertia of motor and the entire system.
J_u, J_{OB} used and observed system inertia.
B damping coefficient.
B_u, B_{OB} used and observed damping coefficients.
θ_m, θ_{mR} position feedback and command.
$\Delta\theta$ position error.
ω_m speed feedback.
i_q, i_{qR} q-axis current feedback and command.
K_t torque coefficient.
T_e, T_L electromagnetic drive torque and load torque.
$P(s)$ control target transfer function.
$G_{PI}(s)$ PI controller transfer function.
$G_{Lead}(s)$ lead-compensator transfer function.
$G_{LPF}(s)$ second-order low-pass filter (LPF) transfer function.
$G_{ACR}(s)$ current loop equivalent transfer function.
$G_h(s)$ zero-order-hold transfer function.
$G_{NF}(s)$ notch filter transfer function.
$C_0(s)$ PI-Lead controller transfer function.
$C_1(s)$ PID controller transfer function.
$L_0(s)$ PI-Leadbased control system.
$L_1(s)$ PID based control system.
$L_2(s)$ P-Lead based control system.
K_{p0}, K_{p1} PI-Lead and PID proportional gains.
K_d PID controller differential gain.
$K_{PI\text{-}Lead}$, K_{PID}, $K_{P\text{-}Lead}$ equivalent open-loop gains of PI-Lead, PID, P-Lead based systems.
ω_{i0}, ω_{i1} PI-Lead and PID integral corner frequencies.
ω_c PI-Lead controller open-loop cut-off frequency.
ω_{cmax} PI-Lead estimated maximum cut-off frequency.
ω_l, ζ cut-off frequency and damping ratio of the LPF.
ω_d current loop cut-off frequency.
ω_n notch frequency of the notch filter.
b_n -3 dB notch bandwidth of the notch filter.
α lead compensator bandwidth factor.
T_m mechanical time constant.
T_c PI-Lead controller cut-off frequency time constant.
T_{i0} PI-Lead controller integration time constant.
T_l LPF cut-off frequency time constant.
T_x, T_y PID controller equivalent time constants.
T_{APR} Position controller discretization period.
A_m controller output limitation value.
$N(X/A_m)$ output saturation nonlinearity describing function.
E_{RMSE} root mean square error.
E_{FRMSE} fast root mean square error.
q_1 tracking back calculation factor.
q_2 system stability margin factor.

Manuscript received February 06, 2021; revised May 06, 2021 and June 18, 2021; accepted July 01, 2021. This work was supported in part by the National Natural Science Foundation of China under Grant 51991385 and in part by the National Key R&D Program of China under Grant 2017YFB1300800. (*Corresponding author: Ming Yang.*)

Yangyang Chen, Ming Yang, Kaiyuan Liu, Jiang Long, and Dianguo Xu are with the School of Electrical Engineering and Automation, Harbin Institute of Technology (HIT), Harbin 150001, China (e-mail: 1120610324@hit.edu.cn; yangming@hit.edu.cn; 20S006054@stu.hit.edu.cn; 16b306004@hit.edu.cn; xudiang@hit.edu.cn).

Frede Blaabjerg is with the Department of Energy Technology, Aalborg University, Aalborg 9220, Denmark (e-mail: fbl@et.aau.dk).

I. Introduction

CONVENTIONALLY, people adopt the classic Proportional-Integral-Derivative (PID) based three-closed-loop structure in servo systems, where a current feedback controller, a speed feedback controller, and a position feedback controller, from the inside out [1]-[4] are applied. However, the error-driven speed controller will cause response delay, and the high-frequency speed control will lead to large quantization noise in speed measurement. Hence, aiming for the best motion control performance, the dual-closed-loop structure (where the speed controller is removed) is preferred in those systems with strict indicators about tracking error and dynamic performance [5], [6], like lithography machines and Lidars. Furthermore, considering the impact from feedback noise will impact the system stability, by using a lead-compensator to replace the derivative term [7]-[9], then the Proportional-Integral-Lead (PI-Lead) position controller is born [10]-[14]. In fact, decades ago, because analog devices and operational amplifiers in the early stage could not realize the ideal derivative function, engineers and scholars always chose to use the PI-Lead controller to replace the PID controller. Thus, the usage history of the PI-Lead controller is not shorter than PID, and PI-Lead is also a simple and useful industrial-level algorithm. For example, Fu *et al.* built an adaptive iterative learning control scheme based on the PI-Lead controller and successfully applied it to a wafer stage [11]. Li *et al.* used the PI-Lead controller plus notch filters to achieve the reset controller's basic structure in a hard disk drive servo system [12]. Besides servo systems, PI-Lead controller was also used in other fields, like battery energy storage systems [13] and boost converters [14].

Similar to other PI-based controllers, the integral part of the PI-Lead controller can lead to windup phenomena. For example, the Lidar servo drive systems, which are used in electric vehicles, can be unstable under the severe impact torque, commonly seen in the standard vibration and impact tests of VOLKSWAGEN 80000. In order to enhance the Anti-Windup (AW) ability of the PID controller, there are several classic solutions, like Conditional Integration (CI) [15], [16], Tracking Back Calculation (TBC) [17], [18], and Integral State Predictor (ISP) [18]-[20]. Besides, as for the AW of the lead compensator, Yang *et al.* proposed an observer-based scheme to reduce the impact from the saturation of the phase-lead/phase-lag controller [21]. However, there are few works that focus on the windup problem of the PI-Lead controller. Because the Direct Current (DC) gain of the lead compensator is not a unit, AW strategies of the PI-Lead controller need to be redesigned and discussed in depth. Without a suitable redesign of the conventional PI-Lead controller structure, the classic AW methods, like CI and TBC, can even make the system fragile and unstable.

Another open issue in PI-Lead controller design is the control parameter optimization, where general performance indexes and tuning rules are lacking. Tursini *et al.* proposed a real-time model-free gain tuning strategy for the PI speed controller based on the difference between the effective overshoot and the ideal one [22]. Cheng and Tzou proposed a fuzzy-logic-based step-size tuning strategy to find out a set of optimal control parameters under predetermined objective functions of the position following error, position overshoot, speed transient response, and corresponding control effort [1]. In [23], by studying a high-performance drilling process and choosing the overshoot and the Integral of weighted Time Absolute Error (ITAE) as cost functions, a real-valued Genetic Algorithm (GA) for optimal PID controller design is achieved. Hsu and Lai, by considering the characteristic of the number of "current slope change," an optimal bandwidth search algorithm is proposed to maximize the performance of classic Proportional and Proportional-Integral (P+PI) form controllers [3]. However, most of the works focus on the PI-based controllers, and there still have room for exploring the PI-Lead controller self-commissioning. Furthermore, in order to protect systems, reducing the oscillation and unnecessary factors during the tuning process is also essential.

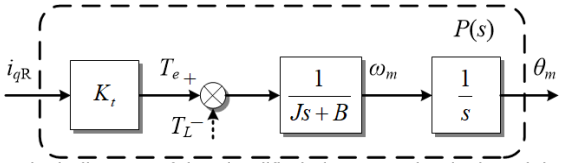

Fig. 1. Block diagram of the simplified electromechanical model.

In this paper, motivated by the above discussions, a reversed-structure-based PI-Lead controller for AW design and a self-commissioning strategy are proposed. First, Section II introduces the linear and nonlinear modeling processes and stable analyses of the classic PI-Lead control system. Analysis results show that the AW algorithm can eliminate the divergence phenomenon of the PI-Lead controller. Then, because the traditional AW methods are unsuitable for the PI-Lead controller with a conventional structure, two specially designed structures for the PI-Lead controller AW problem are proposed in Section III. Next, in Section IV, considering the conventional periodic self-tuning index based on Root Mean Square Error (RMSE) cannot immediately identify the instability and oscillation, an easy-implemented Fast RMSE (FRMSE) index is proposed. The FRMSE can significantly shorten the detection time of the instability. Then, Section V uses experiment results to verify the advantages and effectiveness of the proposed reversed-structure and self-commissioning strategies for the PI-Lead controller. In the last, Section VI gives a summary of this paper.

II. Stability Analysis of the Digital PI-Lead Controller with Output Saturation Nonlinearity

A. Electromechanical Model

Fig. 1 shows the simplified electromechanical model of the targeted servo system. Kinematics equations of the system based on the Surface-mounted Permanent Magnet Synchronous Motor (SPMSM) are illustrated as follows

$$\begin{cases} \mathrm{d}\theta_m/\mathrm{d}t = \omega_m \\ J\,\mathrm{d}\omega_m/\mathrm{d}t = T_e - B\omega_m - T_L \\ T_e = K_t i_q \end{cases} \tag{1}$$

in which, θ_m and ω_m represent the angle and speed of the motor, respectively. J is the equivalent inertia of the entire system. ω_m is dependent on electromagnetic torque T_e, damping coefficient B causes dynamic friction, and T_L is the disturbance torque. Additionally, i_q is the equivalent current in the quadrature direction, and K_t is the torque coefficient.

Then, as shown in Fig. 1 (i_{qR} is the q-axis current reference), the transfer function of the plant $P(s)$ can be expressed as

$$P(s)=K_t/\left(Js^2+Bs\right)=K_t/\left[Bs\left(T_m s+1\right)\right] \tag{2}$$

in which, the mechanical time constant $T_m=J/B$.

The classic PI-Lead controller cascades with a second-order low-pass filter (LPF) $C_0(s)$ can be expressed as

$$C_0(s)=G_{\mathrm{PI}}(s)\times G_{\mathrm{Lead}}(s)\times G_{\mathrm{LPF}}(s)$$
$$K_{p0}\left(1+\frac{\omega_{i0}}{s}\right)\left(\frac{\alpha s+\omega_c}{s+\alpha\omega_c}\right)\left(\frac{\omega_l^2}{s^2+2\zeta\omega_l s+\omega_l^2}\right) \tag{3}$$

in which, K_{p0} is the proportional gain of the PI-Lead controller, ω_{i0} is the corner frequency of its integral term, and α is the bandwidth of the lead compensator. ω_l and ζ represent the cut-off frequency and damping ratio of the second-order LPF. Furthermore, ω_c is the open-loop cut-off frequency of 0 dB.

Then, based on (2) and (3), the open-loop transfer function of the PI-Lead based system $L_0(s)$, and the magnitude equation of the cut-off frequency ω_c can be given as

$$L_0(s)=C_0(s)P(s)$$
$$=\frac{K_{\text{PI-Lead}}\left(T_{i0}s+1\right)\left(\alpha T_c s+1\right)}{s^2\left(T_m s+1\right)\left(T_c s/\alpha+1\right)\left(T_l^2 s^2+2\zeta T_l s+1\right)} \tag{4}$$

$$\left|L_0(s)\right|_{s=\mathrm{j}\omega_c}=\left|C_0(s)P(s)\right|_{s=\mathrm{j}\omega_c}=1 \tag{5}$$

where, the equivalent gain $K_{\text{PI-Lead}}=K_t K_{p0}\omega_{i0}/(\alpha B)$, the integration time constant $T_{i0}=1/\omega_{i0}$, the cut-off frequency time constant $T_c=1/\omega_c$, and the second-order LPF time constant $T_l=1/\omega_l$.

From (5), K_{p0} can be approximately calculated as

$$K_{p0}=\left(J\omega_c^2+B\omega_c\right)/K_t \tag{6}$$

Additionally, the traditional PID cascades with a second-order LPF $C_1(s)$ can be expressed as

$$C_1(s)=K_{p1}\left(1+\frac{\omega_{i1}}{s}+K_d s\right)\left(\frac{\omega_l^2}{s^2+2\zeta\omega_l s+\omega_l^2}\right) \tag{7}$$

in which, ω_{i1} is the integral term corner frequency of the PID controller. K_{p1} and K_d are its proportional gain and differential gain, respectively.

Based on (2) and (4), by transforming the related parameters to equivalent gain and time constants, the open-loop transfer function of the PID controller based system $L_1(s)$ can be given as

$$L_1(s)=C_1(s)P(s)=\frac{K_{\text{PID}}\left(T_x s+1\right)\left(T_y s+1\right)}{s^2\left(T_m s+1\right)\left(T_l^2 s^2+2\zeta T_l s+1\right)} \tag{8}$$

in which, K_{PID} is the equivalent gain of $L_1(s)$, T_x and T_y are equivalent time constants. Then, the related parameters of the PID-based controller can be calculated as

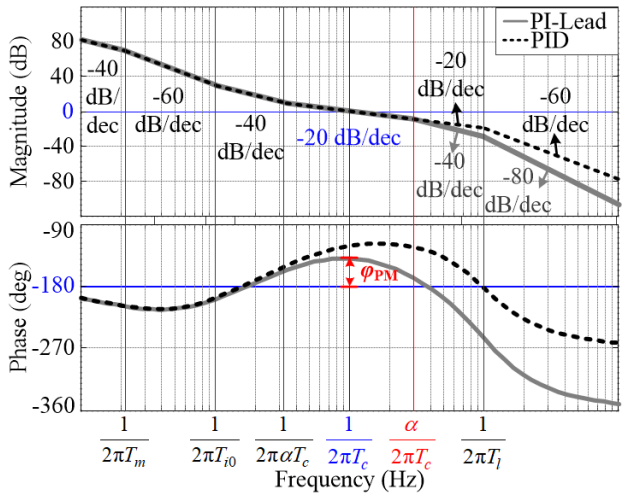

Fig. 2. Bode diagrams of $L_0(s)$ and $L_1(s)$.

$$\omega_{i1}=1/\left(T_x+T_y\right) \tag{9}$$

$$K_d/\omega_{i1}=T_x T_y \tag{10}$$

$$K_{\text{PID}}=K_t K_{p1}\omega_{i1}/B \tag{11}$$

Furthermore, according to the definition of the cut-off frequency ω_c, the value of $K_{p1}K_d$ can be calculated as

$$K_{p1}K_d=\left(J\omega_c+B\right)/K_t \tag{12}$$

If the values of T_x, T_y, and ω_c are predetermined, the parameters of the PID controller, K_{p1}, ω_{i1}, and K_d, can be obtained based on (9) to (12).

In order to compare the PI-Lead and PID controllers, open-loop Bode diagrams of $L_0(s)$ and $L_1(s)$ are shown in Fig. 2, in which φ_{PM} is the Phase Margin (PM) of the PI-Lead controller, the PI-Lead and PID controllers have the similar equivalent gain, crossover frequency, and corner frequencies. In detail, $K_{\text{PI-Lead}}=K_{\text{PID}}$, $T_{i0}=T_x$, $\alpha T_c=T_y$. Compared with PID, the PI-Lead controller has one more open-loop pole, which means better noise reduction ability in the high-frequency band. Besides, the parameters of the PI-Lead controller have more direct relationships with corner frequencies.

B. Stability Analysis of the Digital PI-Lead Controller

According to the linear control theory, if $\varphi_{\text{PM}} > 0$ in Fig. 2, the PI-Lead controller based system is stable. However, the model described by (4) does not consider the impact from the output saturation nonlinearity of the PI-Lead controller, which can cause the limit cycle oscillation. The describing function of the output saturation nonlinearity $N(X/A_m)$ can be given as

$$N(X/A_m)=\frac{2}{\pi}\left[\arcsin(X/A_m)+(X/A_m)\sqrt{1-\left(X/A_m\right)^2}\right] \tag{13}$$

in which, A_m is the output limit value of the PI-Lead controller.

As mentioned in Part I, if the system enters the saturation state, most Anti-Windup algorithms will reduce or eliminate the influence of the integral term. In other words, the function of the Anti-Windup algorithm can be regarded as removing the integral term and changing the controller type from the PI-Lead to the P-Lead when saturation happens. According to (4), remove the integral term and keep the values of other

parameters unchanged, the open-loop transfer function of the P-Lead controller $C_2(s)$ based system $L_2(s)$ can be given as

$$L_2(s) = C_2(s)P(s) = \frac{K_{\text{P-Lead}}(\alpha T_c s+1)}{s(T_m s+1)(T_c s/\alpha+1)(T_l^2 s^2+2\zeta T_l s+1)} \quad (14)$$

in which, $K_{\text{P-Lead}}$ is the equivalent gain of $L_2(s)$.

Then, the liner part transfer functions $L_0(s)$ and $L_2(s)$, and the negative inverse describing function curve $-1/N(X/A_m)$ are plotted in Fig. 3. Based on the Nyquist stability criterion, if a system with no poles located on the right-hand half of the complex plane is stable, its open-loop frequency response cannot encircle the critical point (-1, j0) in the $GH(s)$ plane. Hence, in linear control theory, the $L_0(s)$ and $L_2(s)$ in Fig. 3 (a) are stable, while they are unstable in Fig. 3 (b).

However, according to the describing function method [24], whatever the $L_0(s)$ is stable or not in the linear analysis, it will always have a stable crossover point with the negative inverse describing function curve $-1/N(X/A_m)$. In general, the stable crossover point means the system will fall into a limit cycle, and an oscillation with a constant frequency and amplitude happen, like the $L_2(s)$ in Fig. 3 (b). However, the crossover point frequency of $L_0(s)$ and $-1/N(X/A_m)$ is close to zero. This special frequency means, when the system enters a deep saturation state, the oscillation frequency will get slower and the amplitude will become larger, and then the system will show a divergent form. In contrast, if the PI-Lead controller has the AW function, the AW algorithm will help the controller reduce or remove the integral part when the system is saturated and turn the controller into the P-Lead mode. Then, the divergence phenomenon can be avoided. Hence, besides reducing the overshoot, the AW algorithm has a more significant meaning for the PI-Lead-based dual-closed-loop position control system. Furthermore, it is worth mentioning that the PID-based system $L_1(s)$ also has similar characteristics.

Besides the output saturation of the controller, the influences from the digital control and current response delay also need to be considered. Fig. 4 is the block diagram of the entire control system, where $\theta_{m\text{R}}$ is the position reference. T_d is the equivalent time constant of the current loop, and T_{APR} is the sampling period of the position controller. In this paper, a delay part is used to simulate the delay caused by the non-ideal current control. The phase of the current closed-loop cut-off frequency ω_d is set as $-\pi/4$. Then, the transfer function of the delay-model-based current loop $G_{\text{ACR}}(s)$ can be given as

$$G_{\text{ACR}}(s) = K_t e^{-\frac{\pi}{4\omega_d}s} = K_t e^{-T_d s} \quad (15)$$

in which, T_d is obtained by the current sweep-frequency test.

Furthermore, as a digital system, digital control brings phase lag to the system inevitably. Here, the phase part of the zero-order-hold (ZOH) with time constant T_{APR} is used to simulated the phase lag from the digital control. The transfer function of ZOH $G_h(s)$ can be given as

$$G_h(s) = \left(1-e^{T_{\text{APR}}s}\right)/s \quad (16)$$

From (16), the phase of $G_h(s)$ can be expressed as

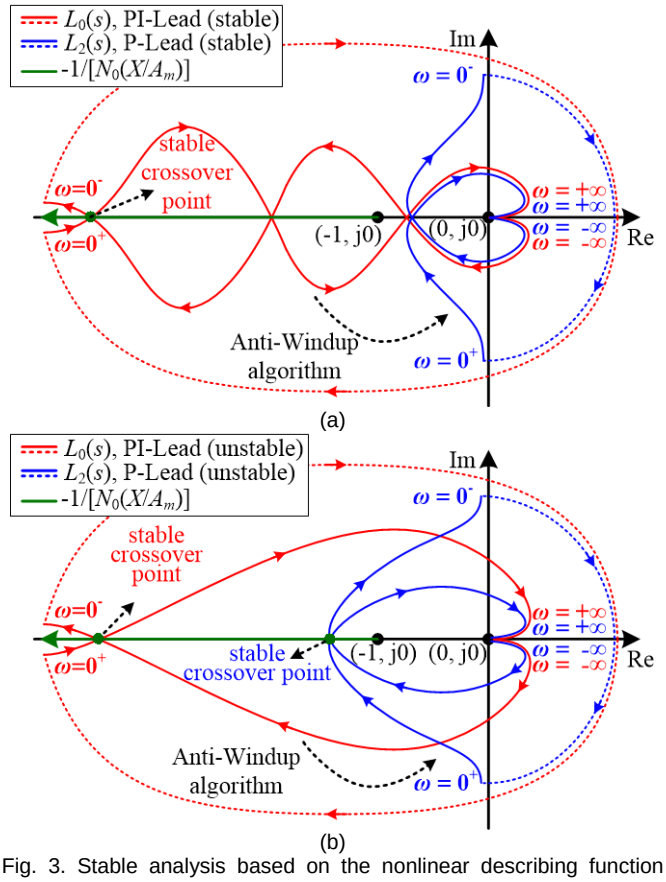

Fig. 3. Stable analysis based on the nonlinear describing function method and Nyquist curve. (a) Systems are stable in the linear model. (b) Systems are unstable in the linear model.

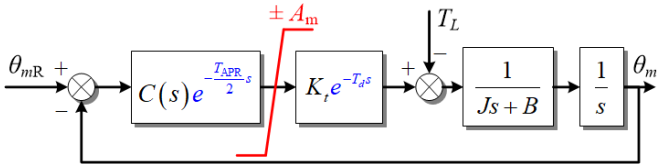

Fig. 4. Block diagram of the entire control system.

$$\angle G_h(\text{j}\omega) = e^{-\text{j}\frac{\omega T_{\text{APR}}}{2}} = -\omega T_{\text{APR}}/2 \quad (17)$$

Based on the symmetry criterion, setting ω_{i0}, ω_l, α, and ζ as

$$\begin{cases} \omega_{i0} = 0.1\omega_c \\ \omega_l = 10\omega_c \\ \zeta = 0.7 \\ \alpha = 9 \end{cases} \quad (18)$$

Then, the Phase Margin (PM) φ_{PM} ($\varphi_{\text{PM}} > 0$) of the system can be expressed as

$$\varphi_{\text{PM}} = \angle G_{\text{PI}}(\text{j}\omega_c) + \angle G_{\text{Lead}}(\text{j}\omega_c) + \angle G_{\text{LPF}}(\text{j}\omega_c) + \angle P(\text{j}\omega_c) + \angle G_{\text{ACR}}(\text{j}\omega_c) + \angle G_h(\text{j}\omega_c) + \pi \quad (19)$$

Then, considering $\omega_c >> B/J$, by submitting (18) into (19), and setting $\omega_{c\max}$ as the maximum cut-off frequency of the PI-Lead controller. Based on (19), $\omega_{c\max}$ can be calculated as

$$\omega_{c\max} \le \frac{2\arctan(\alpha_{\max}) - 0.57\pi - \varphi_{\text{PM}}}{(T_d + T_{\text{APR}}/2)} = \frac{0.36\pi - \varphi_{\text{PM}}}{(T_d + T_{\text{APR}}/2)} \quad (20)$$

In general, based on (6), (18), and (20), if J and B of the system are obtained, all of the PI-Lead controller parameters, except ω_c, can be directly calculated. Because the additional phase delay analysis is just used to modify the calculation of the φ_{PM} and the actual cut-off frequency ω_c is much lower than π/T_{APR} and the current loop bandwidth, the adding of $G_h(s)$ and $G_{ACR}(s)$ will not influence the stability analysis in Fig. 3.

Additionally, although the ω_{cmax} is calculated and can be used as a guide, it cannot be used directly because of the model mismatch and unmodeled factors. Hence, an additional rule-based ω_c search process is needed. Considering a commissioning process exists, the value of J and B can be obtained by many classic identification methods [25]-[27]. The mechanical parameter identification process and the search rule of ω_c will be discussed in Part IV.

III. The Proposed Reversed-Structure-Based PI-Lead Controller for the Anti-Windup Design

As for a digital controller, the output saturation part is essential because the affordable current and the nominal current of inverters and motors are predetermined. Fig. 5 (a) shows the conventional saturation part location in the traditional PI-Lead controller (saturation structure one, SS1, conventional structure). An output limitation, with saturation values $\pm A_m$, is put after the final output of the controller.

However, just adding a limitation part is not enough. The nonlinear saturation characteristics can lead to another new problem. For example, the windup phenomenon caused by the integration and output limitation can degrade the control performance, result in a high overshoot and long settling time, and even cause system instability. As mentioned before, two types of classic Anti-Windup (AW) methods, Conditional Integration (CI) and Tracking Back Calculation (TBC) [15]-[19], are shown in Fig. 6, in which i_{qR0} is the middle current reference and q_1 is the gain factor of the TBC ($q_1 > 0$, in this paper, $q_1 = 0.1$ is used for verification). Although these two methods are useful, they need the PI controller to have its own output saturation part. Thus, the CI and TBC cannot be realized in SS1.

Fig. 5 (b) shows the most straightforward way to meet this requirement (saturation structure two, SS2, dual-limitation), in which another $\pm A_m$ saturation is added after the PI controller. However, this structure does not consider the impact of the lead compensator. When the output of the PI controller enters the saturation range, the input of the lead compensator turns to a direct current (DC) component, $\omega = 0$, then the DC gain of the lead compensator can be given as

$$\left|G_{\text{Lead}}(j\omega)\right|_{\omega=0} = (0+\omega_c)/(0+\alpha\omega_c) = 1/\alpha \tag{21}$$

From (21), because of $\alpha > 1$, the output current reference decreases dramatically when the saturation happens.

In this part, two kinds of modified saturation structures are proposed. The first type, saturation structure three (SS3, modified dual-limitation), is shown in Fig. 5 (c), in which the saturation values are changed from $\pm A_m$ to $\pm \alpha A_m$ to keep the controller operating normally during the saturation state.

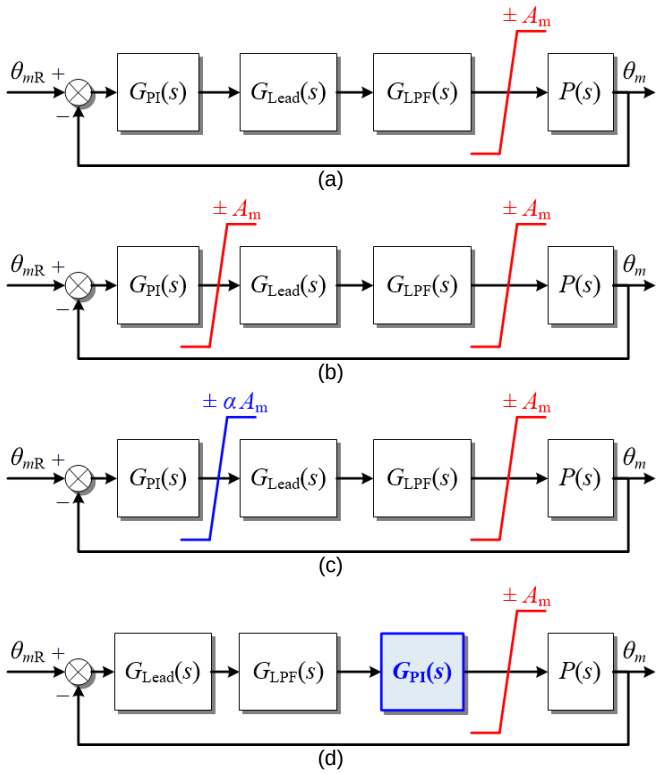

Fig. 5. Four kinds of saturation structures. (a) Saturation structure one (SS1, conventional structure). (b) Saturation structure two (SS2, dual-limitation). (c) Saturation structure three (SS3, modified dual-limitation). (d) Saturation structure four (SS4, reversed structure).

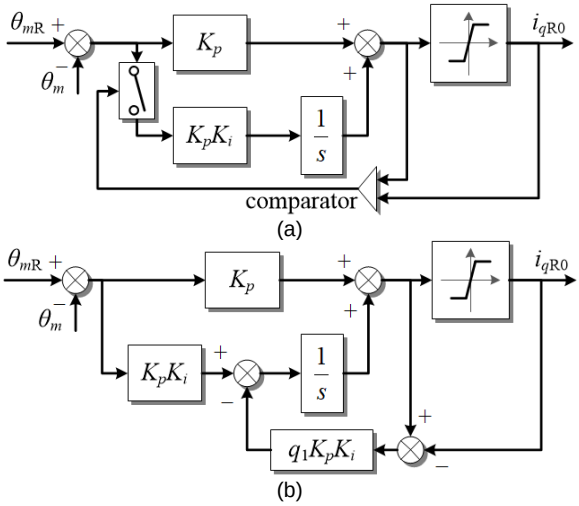

Fig. 6. Two types of classic anti-windup methods [15]-[19]. (a) Conditional integration (CI). (b) Tracking back calculation (TBC).

As for the second modification type, in Fig. 5 (d), the saturation structure four (SS4, reversed structure) chooses to rearrange the cascade order of the PI-Lead controller. Because the first block PI controller is moved to the last, SS4 just needs one saturation part and does not need to adjust the saturation value. Additionally, because the limitation value of the SS4 is much smaller than SS3, the SS4 has stronger stability and fast desaturation speed. The detailed experimental comparison results of these four saturation structures mentioned above will be given in Part V.

IV. Fast RMSE based Self-Commissioning Rule

A. Fast RMSE based Index

Fig. 7 is the commissioning process. During this whole process, the crossover frequency ω_c of the PI-Lead controller is increasing. The gray line is the position command, while the different blue lines are the position feedback of different controller gains. The blue arrows mean the end of each tuning period and controller adjustment for time-domain indexes. As shown in Fig. 7, the controller performance will be changed from soft to moderate, and then from suitable to unstable at last, with the increasing of the controller gain. Hence, one of the most straightforward tuning strategies is to find out the critical gain when the first time that the system comes to the critical stability or instability state, like the classic manual Ziegler-Nichols tuning method.

The first step to detecting the instability is to choose an index to evaluate the control performance of the parameter in use. In this paper, the position error $\Delta\theta$ is selected as the basic signal input for bandwidth searching.

$$\Delta\theta = \theta_{m\mathrm{R}} - \theta_m \tag{22}$$

Then, the classic Root Mean Square Error (RMSE) E_{RMSE} is used as the performance index ($\Delta\theta(i)$ is the input error of the i-th point, and m is the point number in one tuning period).

$$E_{\mathrm{RMSE}} = \sqrt{\frac{1}{m}\sum_{i=1}^{m}\Delta\theta(i)^2} \tag{23}$$

Under the premise of stability, a higher controller gain means a smaller average tracking error (because of the smooth commissioning trajectory planning, the impact from the overshoot is reduced in some sense). However, as the higher the open-loop gain in time-delayed systems, the smaller stability margins become, and the system might become unstable in general, or fall into a limit cycle when saturations are present in the forward loop. Thus, like the red arrow in Fig. 7, the first dramatically E_{RMSE} rebound following with the increase of ω_c in the n-th period can be regarded as the sign of instability, and the condition can be expressed as

$$E_{\mathrm{RMSE}}(n) > E_{\mathrm{RMSE}}(n-1)\ ,\ n>1 \tag{24}$$

However, the E_{RMSE} calculation is at the end of each period. It means that, in the last round of self-commissioning, the system will be in a state of unstable for a whole period, and the severe oscillation may cause damage to the equipment.

In order to accelerate the instability detection, in this paper, a Fast RMSE (FRMSE) index E_{FRMSE} is designed as

$$E_{\mathrm{FRMSE}} = \sqrt{\frac{1}{m}\sum_{i=1}^{k}\Delta\theta(i)^2}\ ,\ k\le m \tag{25}$$

At the end of each period, E_{FRMSE} equals E_{RMSE}.

$$E_{\mathrm{FRMSE}}(n,m) = E_{\mathrm{RMSE}}(n)\ ,\ n\ge 1 \tag{26}$$

$$E_{\mathrm{FRMSE}}(n,k) \le E_{\mathrm{FRMSE}}(n,m)\ ,\ n\ge 1,\ k\le m \tag{27}$$

Different from E_{RMSE}, E_{FRMSE} can be used for instability detection at every moment of each period. As for the error rebound phenomenon, because of the existence of (26) and (27), the condition (24) can be rewritten as

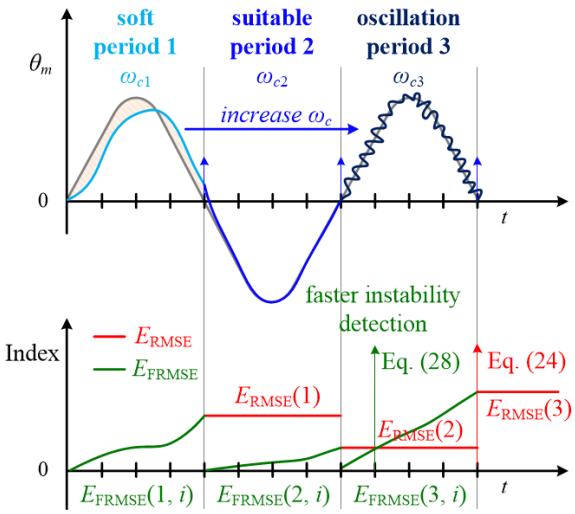

Fig. 7. The simulation working condition for the quantization error analysis and the operating principle of RMSE and FRMSE.

$$E_{\mathrm{FRMSE}}(n,k) > E_{\mathrm{RMSE}}(n-1)\ ,\ n>1 \tag{28}$$

Compared with E_{RMSE} based error rebound condition, the proposed E_{FRMSE} based indicator can reduce the unnecessary waiting time from the k-th point to the m-th point. Like the green line in Fig. 7, because the value of E_{FRMSE} grows fast when the system is unstable, E_{FRMSE} based condition (28) can achieve faster instability detection than the conventional E_{RMSE} based condition (24).

B. Mechanical Parameters Identification

1) Inertia and Damping Coefficient Identification

Before the model identification process, the controller tuning process needs to be conservative because the characteristics of the control target are uncertain. Most of the time, the controller only has the value of the motor inertia J_m ($J > J_m$). It means the control performance during the identification process is not ideal. Thus the identification algorithm needs to face challenges of slower acceleration and larger feedback noise. Considering the trajectory of the Lidar servo is a repeatable rotation, the adopted identification strategy is based on a classic identification process in the form of integration. The estimation equations of inertia and damping coefficient can be given as [3], [4], [25]

$$J_{\mathrm{OB}} = \int_{t_1}^{t_2} T_e \frac{\mathrm{d}\omega_m}{\mathrm{d}t}\mathrm{d}t \Big/ \int_{t_1}^{t_2}\left(\frac{\mathrm{d}\omega_m}{\mathrm{d}t}\right)^2 \mathrm{d}t \tag{29}$$

$$B_{\mathrm{OB}} = \int_{t_1}^{t_2} \frac{\mathrm{d}T_e}{\mathrm{d}t}\frac{\mathrm{d}\omega_m}{\mathrm{d}t}\mathrm{d}t \Big/ \int_{t_1}^{t_2}\left(\frac{\mathrm{d}\omega_m}{\mathrm{d}t}\right)^2 \mathrm{d}t \tag{30}$$

in which, J_{OB} and B_{OB} are observed inertia and damping coefficient, t_1 and t_2 are the start and end times of one period.

2) Mechanical Resonance Frequency Search

As mentioned in Part I, the aim of the dual-closed-loop position control structure is to pursue extremely high motion control accuracy and dynamic performance to meet the requirements of those precision equipments. The mechanical and structural designers of these systems will use different methods to reduce the impact of potential mechanical resonance, such as reinforce the frame of the Lidar lens and

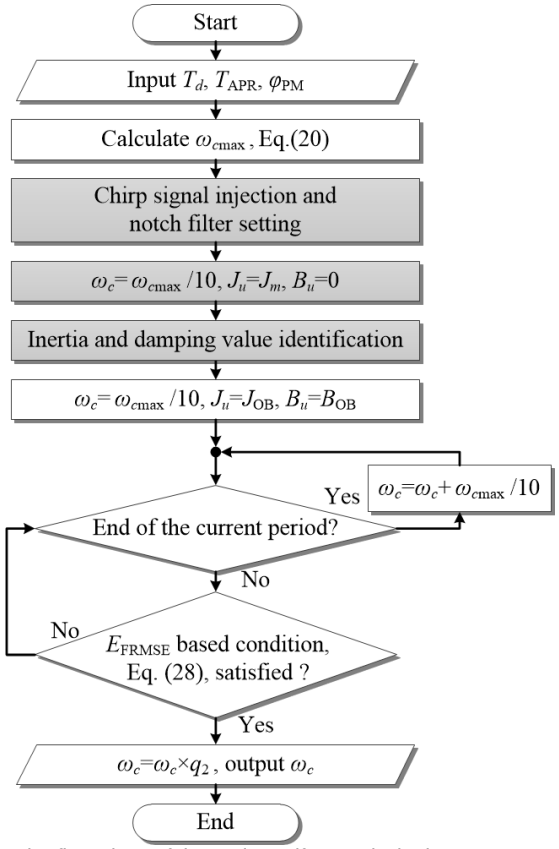

Fig. 8. The flow chart of the entire self-commissioning strategy.

adopted those couplings and shafts with higher stiffness coefficients. Then, the mechanical resonance frequencies of these systems will be pushed to the higher frequency band, which is far away from the operation section, and the mechanical resonance will not have an essential impact on the analysis results in Part II and Part III. In order to further eliminate the effect of the mechanical resonance, the mechanical resonance damping method based on the classic sweep frequency algorithm is used here [28], [29]. In this paper, the *q*-axis chirp current signal, which has an increasing frequency and constant magnitude, is adopted to identify the mechanical resonance frequency of the system f_r. After the f_r is obtained, the mechanical resonance can be damped by adding a traditional notch filter $G_{NF}(s)$, which can be expressed as

$$G_{NF}(s)=\left(s^2+\omega_n^2\right)\Big/\left(s^2+b_n s+\omega_n^2\right) \tag{31}$$

in which ω_n is the notch frequency, and b_n is the -3dB rejection bandwidth factor. As for normal applications, set $\omega_n=2\pi f_r$ and $b_n=\omega_n$ can cope with most situations (especially, the resonance characteristic of the discussed system is weak).

C. Design of the Self-Commissioning Process

Then, based on the digital PI-Lead controller stability analysis, the mechanical parameter identification algorithms, and the E_{FRMSE} based bandwidth searching rule, the flow chart of the entire self-commissioning strategy in Fig. 8 can be obtained. In Fig. 8, the J_u and B_u are the used inertia and damping coefficient for the controller tuning, q_2 is the margin factor ($0<q_2<1$). By referring to the classic Ziegler-Nichols tuning method, q_2 = 0.6, in this paper. If the detailed mechanical parameters of the model have been obtained in advance, users can choose to skip the identification process (the gray blocks). Additionally, because ω_{cmax} only influences the self-commissioning step size and the final value of ω_c depends on the FRMSE searching index, if T_d is uncertain, the ω_{cmax} can be fixed as $200\times2\pi$ rad/s.

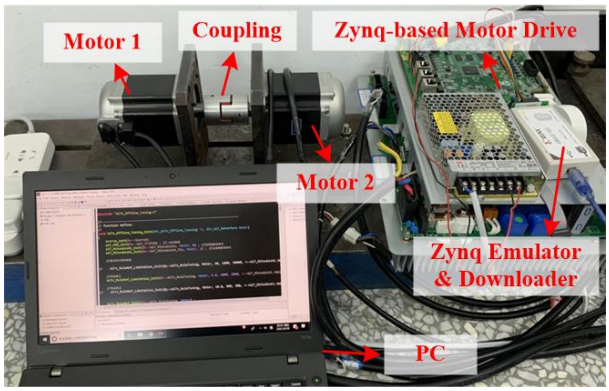

Fig. 9. Experimental platform.

TABLE I
MAIN PARAMETERS OF THE SYSTEM

Parameter	Value
Motor Power P_N	750 W
Nominal Torque T_{eN}	2.39 N·m
Nominal Speed ω_N	3000 r/min
Nominal Current I_N	5×1.414 A
Output Saturation Value A_m	5×1.414 A
Current Loop Time Constant T_d	1.35e-4 s
Current Control Period T_{ACR}	5e-5 s
Position Control Period T_{APR}	2e-4 s
Data Sampling Period T_{sample}	2e-4 s
Phase Margin φ_{PM}	π/4 rad
Maximum Cut-Off Frequency ω_{cmax}	234×2π rad/s
Motor Inertia J_m	1.06e-4 kg·m^2
Reference System Inertia J	2.807e-4 kg·m^2

V. EXPERIMENTAL RESULTS

The self-tuning strategy experiment platform is shown in Fig. 9. Two 750 W TAMAGAWA TS4614N2680 SPMSM equipped with 2^{17} bit encoders are used as the drive and load side motors, respectively, and a rigid coupling connects them. Two motors are fed by one Zynq-based servo drive. Detailed parameters of the servo drive system and controller are presented in Table I. The standard inertia is estimated by the classic off-line identification method with an ideal trajectory and acceleration. About the Zynq-based motor driver, the control chip is Xilinx Zynq series System on Chip (SoC), Zynq7020, which integrates two Advanced Reduced instruction set computing Machines (ARMs) and one Field Programmable Gate Array (FPGA) into one chip. The program is built by Xilinx Software Development Kit (SDK).

TABLE II
MAIN PARAMETERS OF THE USED TRAJECTORIES

	Fast S-Curve	Slow S-Curve
$\{\omega_m\}_{max}$ (rad/s)	80	40
$\{d\omega_m/dt\}_{max}$ (rad/s^2)	600	60
$\{d^2\omega_m/dt^2\}_{max}$ (rad/s^3)	120000	120000
Trajectory Period (s)	1	4

The communication between ARM and FPGA is realized by Advanced eXtensible Interface (AXI) bus inside SoC. Besides, the RAM of Zynq is extended to 1GB by adding an external memory chip to record experiment data. The FPGA is responsible for the current loop control (the classical PI controller is used), while the position controller is finished in ARM. After each turn of the experiment is finished, the Personal Computer (PC) can read the experimental data from RAM through the emulator and Universal Asynchronous Receiver/Transmitter (UART) protocol.

Additionally, the classic S-curve trajectory planning is used for generating the verification trajectory. In the experiment, two kinds of S-curve trajectory planning results, the 'fast S-curve' and the 'slow S-curve,' are used, and their detailed parameters are recorded in Table II.

A. *The Verification of the Proposed Modified Structures for Classic Anti-Windup methods Realization*

First, Fig. 10, Fig. 11, and Fig. 12 show the anti-disturbance test results of different methods and situations.

In this part, the 'fast S-curve' is used in all the position control experiments. The tracking error index E_{RMSE} is used to evaluate the performance of each period. As for the controller, there have J_u=2.807e-4 kg·m^2, B_u=3.766e-3 N·m·s/rad, f_c = f_{cmax}/2=117 Hz (ω_c=2πf_c), and the notch filter is not added. Two kinds of test modes are used for the analysis verification.

The first one is the 'on load start-up.' It simulates the Lidar servo start-up process with frozen lubricants or water in winter or the motor stall state. In Fig. 10 (a), Fig. 11 (a), and Fig. 12 (a), a 2.39 N·m rate load torque T_{eN} is added at the beginning and withdrew at the end of the first second. Especially, because of the back electromotive force (EMF), the load torque of the SS2 is slightly different. However, the failure mechanism is still can be verified.

The second type is the 'trajectory synchronization.' Automatic drive systems of vehicles need several Lidars to work in the synchronous state. Thus, the master controller sends standard trajectory phase marks to sub-controllers of different Lidars for the trajectory correction and synchronization at set intervals. Then, because Lidars have to respond to the command immediately, sub-controllers need to switch their trajectories, which causes a 'trajectory disturbance.' In Fig. 10 (b), Fig. 11 (b), and Fig. 12 (b), a +π rad trajectory switching is used for recurring this problem.

Fig. 10 shows the anti-disturbance performance of the P-Lead controller. Because the P-Lead controller does not have an integral part, both the systems in Fig. 10 (a) and Fig. 10 (b) can return to normal operation after a short time of saturation. In contrast, as for the PI-Lead controller in Fig. 11. When a long time of saturation happens, the system with SS1 turns to a divergent state because of the unlimited growth of the

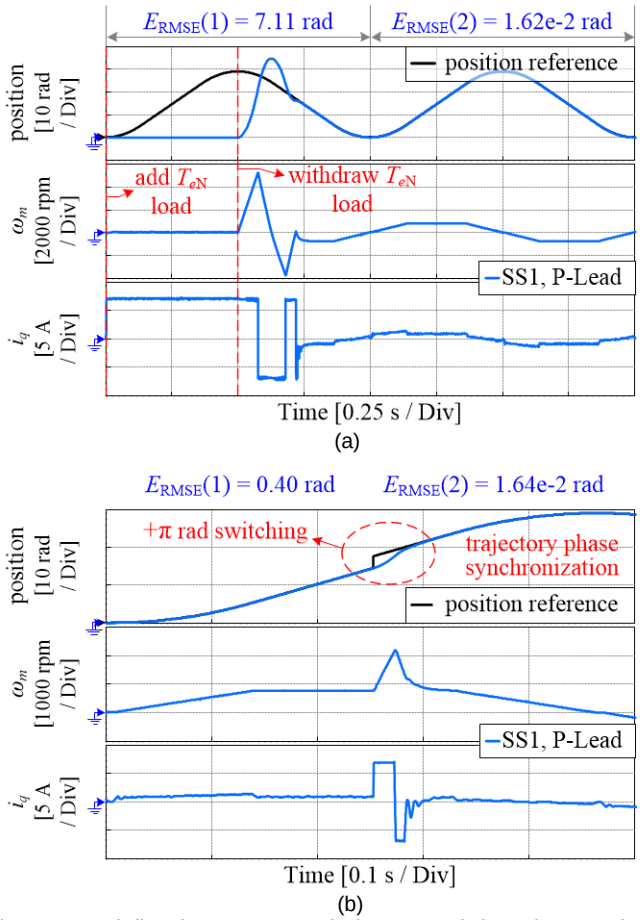

Fig. 10. Anti-disturbance tests of the P-Lead based saturation structure one (without AW). (a) On load start-up, with switching T_{eN} load. (b) Trajectory synchronization, with +π rad command switching.

integral term. Besides, the unsuitable output saturation value of the PI part in SS2 causes the elimination of the PI control performance and makes the system work under a pure wrong saturation state (i_q = A_m / α = 0.79 A, although the PI-Lead SS2 based controller cannot work properly, its load torque command and trajectory state are still same with others).

The performance of the proposed saturation structure three (SS3, modified dual-limitation) and saturation structure four (SS4, reversed structure) are shown in Fig. 12. Especially, the dotted lines in Fig. 12 are the calculated control signal of the PI block without saturation i_{qAW}. In Fig. 12, both the CI-based SS3 and SS4 can make the system work stably after the load switching, but the reversed-structure-based SS4 has better performance and is easier to implement. For example, in Fig. 12 (a), E_{RMSE} of the first and second periods of the CI-based SS3 are 7.87 rad and 1.34 rad, but that of the CI-based SS4 are successfully decreased to 7.05 rad and 1.89e-3 rad. Compared with the CI-based SS3, both the CI-based and TBC-based SS4 can eliminate the impact of the switching load in the first period. The results of the CI-based and TBC-based SS4 are close. As shown in Fig. 6, because the TBC method can automatically reduce the residual integral value when the system is saturated, it has better performance in those system has longer saturation time, such as the condition in Fig. 12 (a).

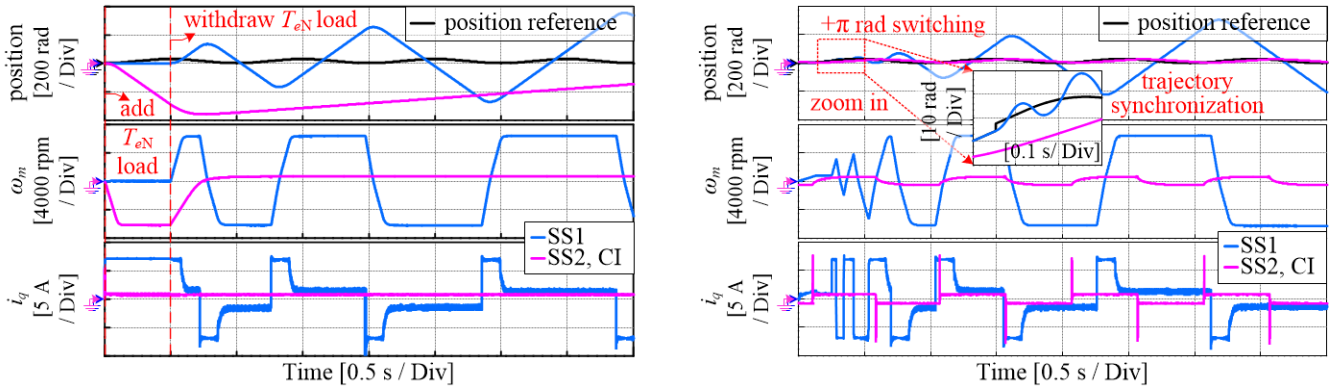

Fig. 11. Anti-disturbance tests of the PI-Lead based saturation structure one (SS1, without AW) and saturation structure two (SS2, dual-limitation). (a) On load start-up, with switching T_{eN} load. (b) Trajectory synchronization, with +π rad command switching.

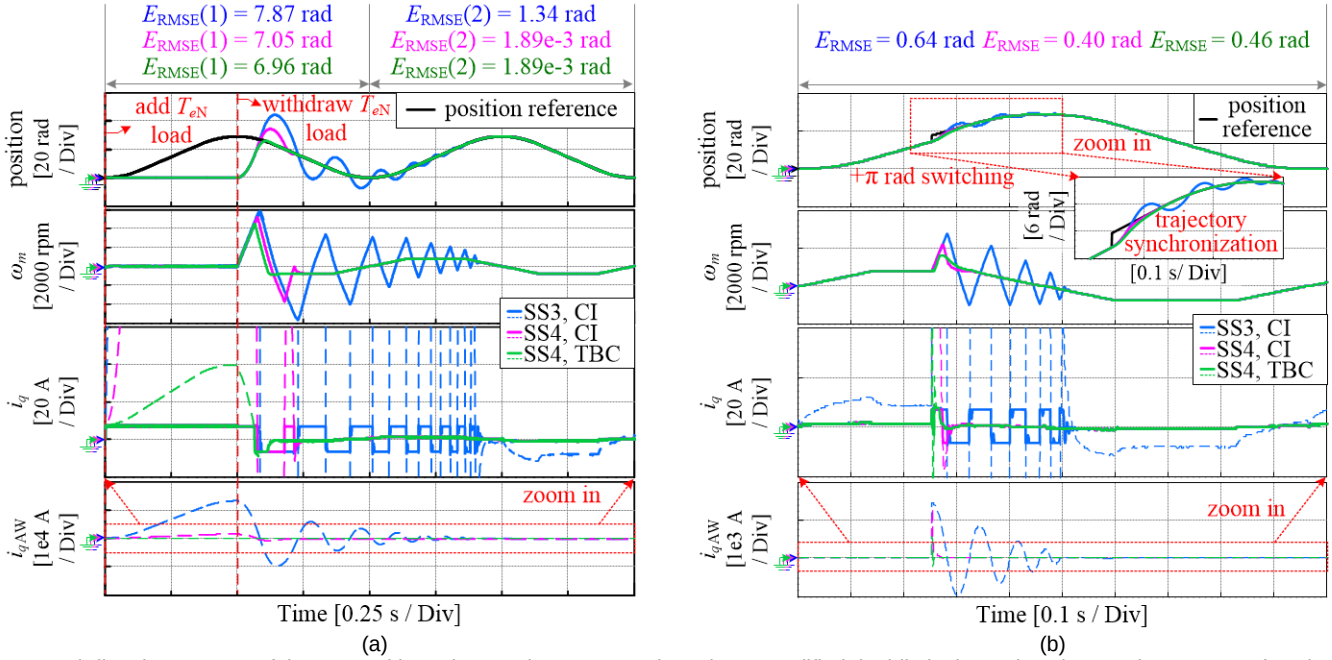

Fig. 12. Anti-disturbance tests of the PI-Lead based saturation structure three (SS3, modified dual-limitation, CI) and saturation structure four (SS4, reversed structure, CI and TBC). (a) On load start-up, with switching T_{eN} load. (b) Trajectory synchronization, with +π rad command switching.

Additionally, anti-disturbance tests of the PID controller are shown in Fig. 13 and Fig. 14 (the PID and PI-Lead controllers have the same corner frequencies and key parameters). In Fig. 13, similar to the PI-Lead-based SS1, the PID-based SS1 appears to diverge after the load torque was withdrawn due to no AW method is adopted. In Fig. 14, by removing integral terms like the P-Lead, the PD controller can work normally, but its tracking error ($E_{RMSE}(2)$ = 8.40e-3) is larger than the PID controller ($E_{RMSE}(2)$ = 1.82e-3). Because the PID controller does not have the lead-compensator, there is no obvious effect by just changing the location of the PID block and the LPF block.

In order to prove the potential value of the reversed structure for the PID controller, the classic step command test in the speed control mode is shown in Fig. 15 (the speed closed-loop bandwidth is 117 Hz, the phase margin is 75 deg, and the cut-off frequency of the LPF is 250 Hz). As for the traditional dual-limitation structure (SS2), although the PID block can enter the saturation state at the very beginning and want to output a maximum torque, the actual torque command – the output of the LPF cannot rise rapidly. In contrast, because the output of the PID block is the final output of the entire controller in the proposed reversed structure (SS4), the drive torque can reach the maximum value immediately and can achieve faster desaturation. Overall, the key factor that makes the difference between the classic dual-limitation and proposed reversed structure is that the reversed structure only has one output limitation in the forward loop.

In general, the experimental results in this part successfully verify the stable analysis in Part II and the effectiveness of the proposed structures in Part III. Not only the PI-Lead controller, the nonlinear stability analysis and the proposed reversed structure can also be applied to the PID controller. In the following commissioning process, the combination of the

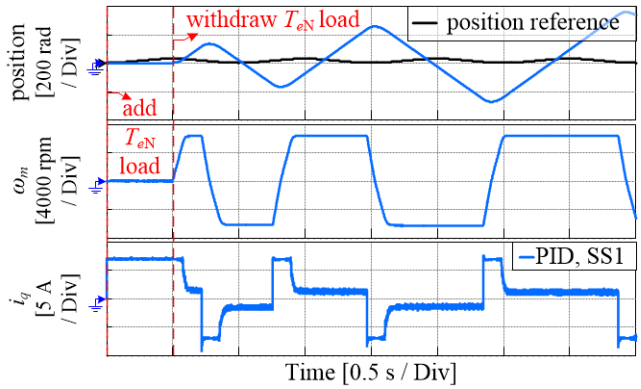

Fig. 13. The anti-disturbance test result of the PID based SS1 (without AW) under switching T_{eN} load.

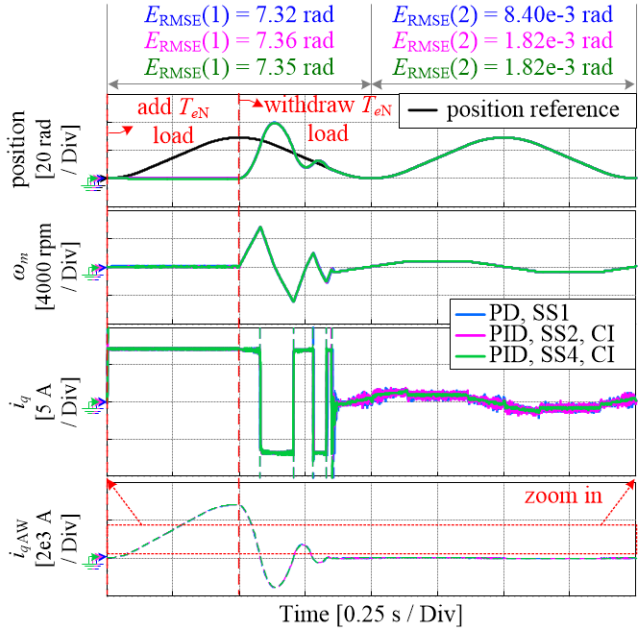

Fig. 14. Anti-disturbance test results of the PD based SS1, PID based SS3 and SS4 under switching T_{eN} load.

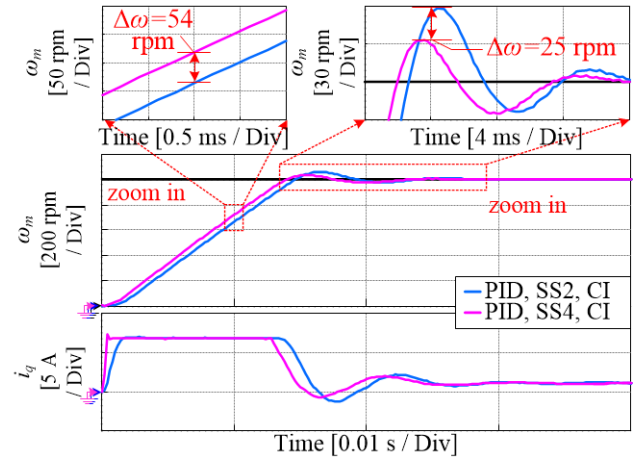

Fig. 15. The 1000 rpm speed step command test of the PID based SS2 (dual-limitation) and SS4 (reversed structure).

TBC method and the proposed reversed-structure-based PI-Lead controller (SS4) is adopted as the tuning object.

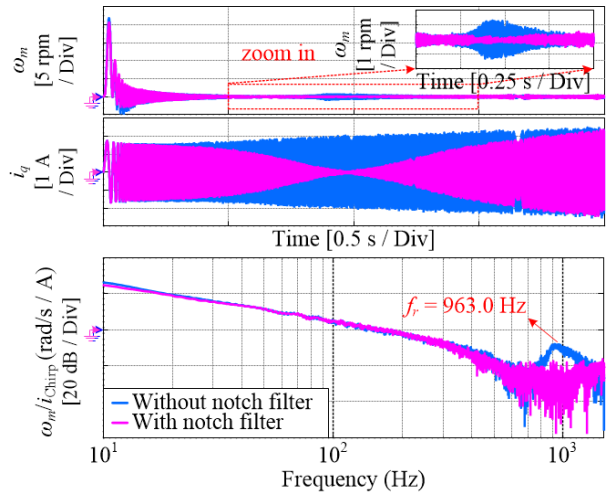

Fig. 16. The Chirp signal based resonance frequency identification and the performance of the notch filter.

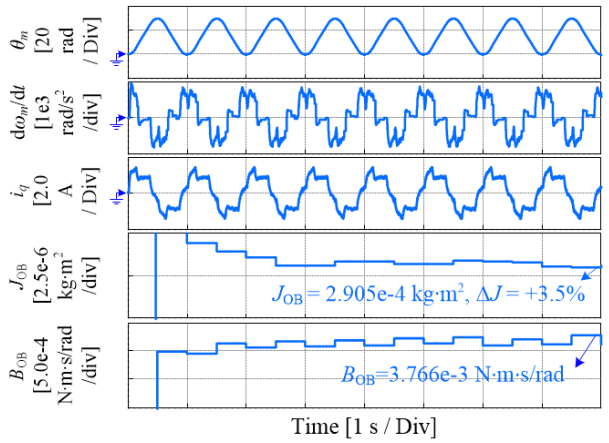

Fig. 17. Inertia and damping coefficient identification results under the same fast S-curve trajectory.

B. Mechanical Parameters Identification

The first step of the mechanical parameter identification is the resonance frequency search. In Fig. 16, a 2 seconds chirp signal is used for identification. Its magnitude is 0.25 I_N, start and end frequencies are 10 Hz and 2000 Hz respectively. The blue line shows that the resonance frequency of the system is 963 Hz, but the resonance magnitude is not obvious because the system in Fig. 9 used a rigid coupling. Then, by adding a corresponding notch filer (ω_n=2π×963 rad/s and b_n=ω_n), the resonance point is eliminated in the purple line.

Next, after added a notch filter, the 'fast S-curve' is used for inertia and damping coefficient identification tests. As for the controller, there have $f_c = f_{cmax}/10 = 23.4$ Hz, $J_u = J_m = 1.06\text{e-}4$ kg·m^2, $B_u = 0$ N·m·s/rad. Fig. 17 shows inertia and damping coefficient identification results under the same fast S-curve trajectory. The inertia identification error is 3.5%, which is very close to the reference value.

C. Fast RMSE based Self-Commissioning

In this part, both the 'fast S-curve' and 'slow S-curve' are used. As for the controller, the parameter tuning process is according to the flow chart in Fig. 8.

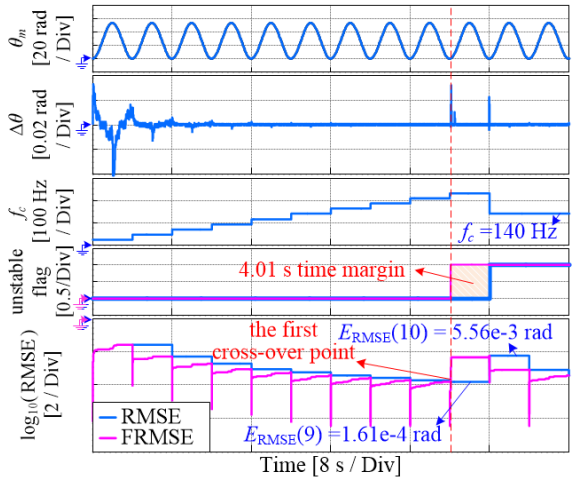

Fig. 18. The RMSE and fast RMSE results variation trend of the same slow S-curve tuning process.

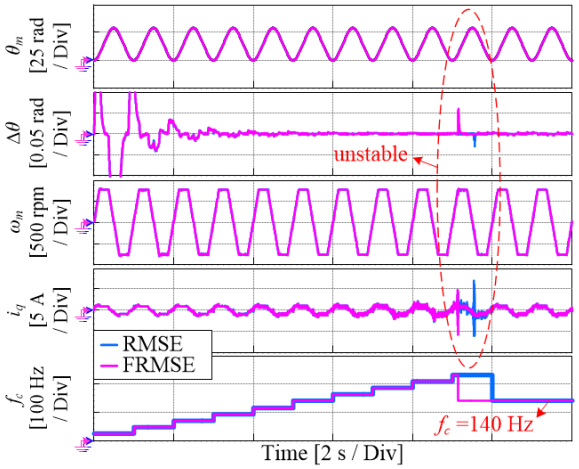

Fig. 19. The comparison results of RMSE and fast RMSE based auto-tuning methods under the same fast S-curve trajectory.

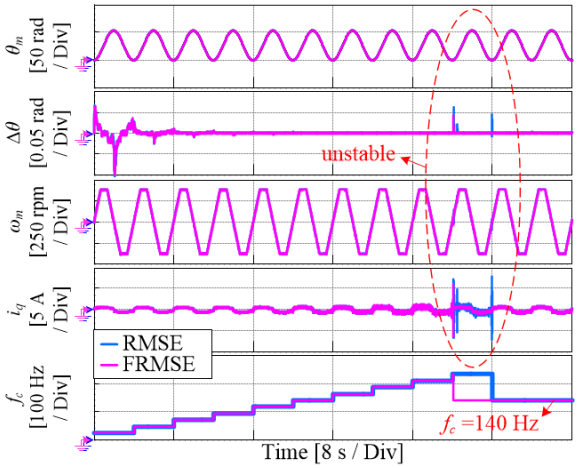

Fig. 20. The comparison results of RMSE and fast RMSE based auto-tuning methods under the same slow S-curve trajectory.

First, in order to verify the error variation trend analyzed in Fig. 7, the comparison results of RMSE and fast RMSE based self-commissioning methods under the same slow S-curve trajectory are recorded in Fig. 18. The values of E_{RMSE} and E_{FRMSE} are shown in the form of $\log_{10}(E_{\mathrm{RMSE}})$ and $\log_{10}(E_{\mathrm{FRMSE}})$. In Fig. 18, the excepted cut-off frequency of the PI-Lead controller f_c is increased from 23.4 Hz to 140.4 Hz. In the 10th period, f_c increases to 234 Hz, and oscillation happens. Compared with $E_{\mathrm{RMSE}}(9)$, the $E_{\mathrm{RMSE}}(10)$ rebounds significantly from 1.61e-4 rad to 5.56e-3 rad. Dislike E_{RMSE}, the results of the proposed real-time calculated index fast RMSE E_{FRMSE} snowballs, and the first time crossover of the E_{RMSE} and E_{FRMSE} happens, which means (28) is satisfied and the controller gain can be adjusted immediately.

The tuning processes under the fast S-curve and slow S-curve, Fig. 19 and Fig. 20, also prove that the proposed fast RMSE index can quickly detect the instability and avoid the long-time unstable of the system. Both the searched cut-off frequencies of fast and slow curves are 140 Hz.

D. *The Performance of Self-Commissioning Results and the Comparison between PI-Lead and PID*

Although the focus of this paper is the PI-Lead controller, the proposed self-commissioning process based on FRMSE can also be used for the tuning of the classic PID controller. In order to verify the adaptability of the FRMSE and make a comparison between the PI-Lead and PID controllers, besides the default setting (α=9, with LPF), another mode, α=3, without LPF, is used for the self-commissioning test. Results are shown in Fig. 21 and Fig. 22. The decrease of α can increase the controller gain in the low-frequency band and enhance the low-pass filter property of the PI-Lead controller itself. The PID and PI-Lead controllers have the same corner frequencies and key parameters based on (4) and (8).

First, the fast S-curve self-commissioning results of the PID and PI-Lead are given in Fig. 21. As for the default setting (α=9, with LPF), both the tuning results of the PID and PI-Lead controllers are 140 Hz in Fig. 21 (a). Furthermore, the minimum tracking error E_{RMSE} of the PID controller is slightly better than PI-Lead, because the PID controller has one less open-loop pole (which means larger phase margin and faster dynamic response). However, it also means the PI-Lead controller has better high-frequency noise suppression ability. Thus, when the setting changed to α=3, without LPF, compared with the PI-Lead, larger noises appear in the current feedback i_q of the PID in Fig. 21 (b).

Additionally, in Fig. 21 (b), the final f_c of the PID is decreased to 112 Hz due to the impact of the noise (part of it comes from the quantization error of the encoder). Compared with the default setting, the minimum tracking error E_{RMSE} of the PID increases to 3.028e-4 rad, while that of the PI-Lead successfully decreases to 1.825e-4 rad. Similar results can also be found in Fig. 22. Both the tracking error and the position deviation under switching load torque of the tuned controller are reduced significantly. When using default self-commissioning results, performances of the PID and PI-Lead controllers are close. However, following the decreasing of α and the removal of the LPF, the searched f_c of the PID is reduced to 112 Hz. Furthermore, although the PI-Lead controller has larger f_c (140 Hz) and better dynamic and steady-state performances in this situation, its current harmonics are still smaller than the PID (f_c = 112 Hz).

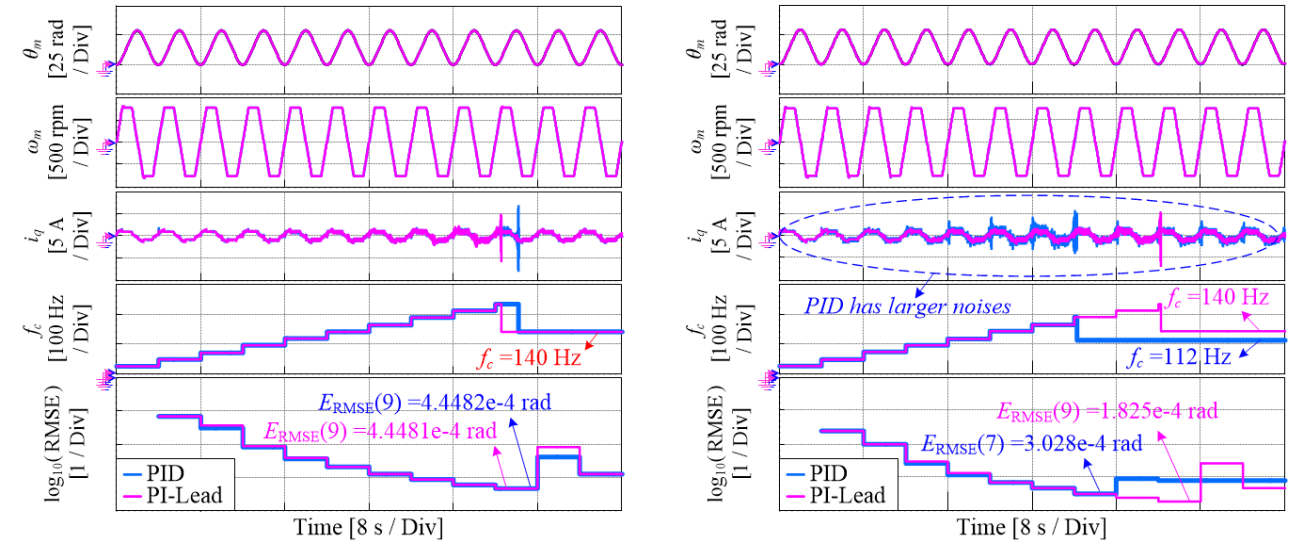

Fig. 21. The comparison of the PID and PI-Lead self-commissioning results under fast S-curve trajectories. (a) α=9, with LPF. (b) α=3, without LPF.

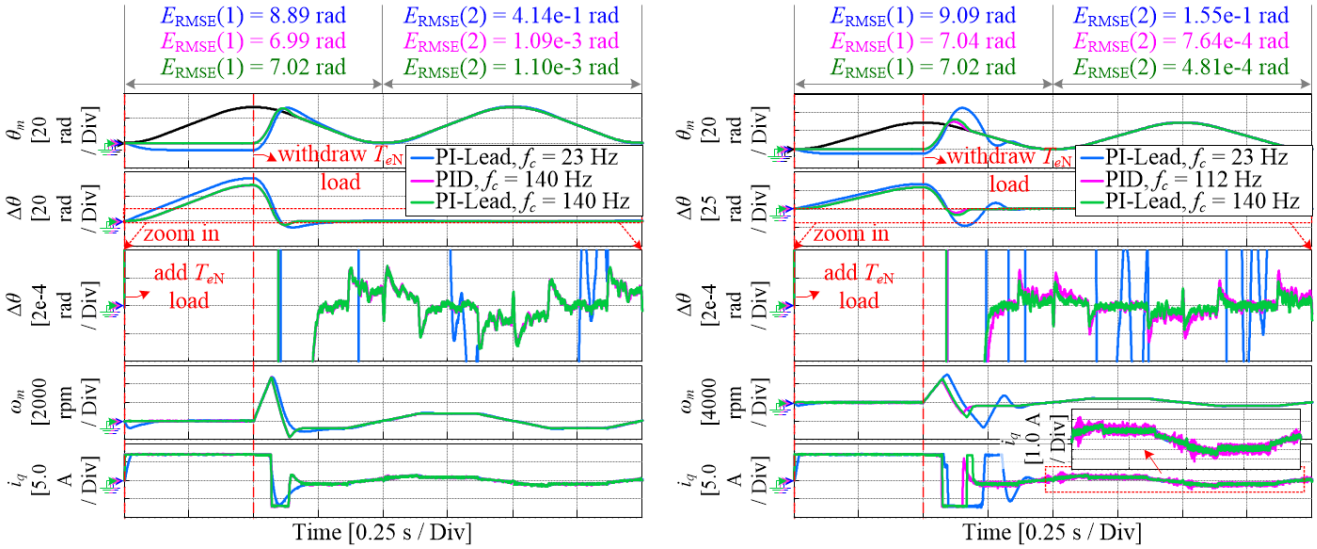

Fig. 22. Anti-disturbance and tracking error test results of the original PI-Lead, the tuned PID and PI-Lead. (a) α=9, with LPF. (b) α=3, without LPF.

VI. Conclusion

In order to achieve better dynamic performance, based on the PI-Lead controller, this paper built up a comprehensive model of the dual-closed-loop position control system. Both the linear and nonlinear stability analyses of the system are finished. According to the analysis results of the nonlinear describing function method, the AW algorithm can reduce the overshoot and ensure that the dual-closed loop position control system does not enter the divergent state. Then, this paper proposed a novel reversed-structure-based redesign method for the conventional PI-Lead controller, which can effectively avoid the failure of traditional anti-windup strategies and make the system work stably under drastic working conditions with the extreme disturbance impact torque (like the vehicle-used Lidar servo drive system). Next, an instability detection method based on the FRMSE is proposed. A simple PI-Lead controller self-commissioning process without additional manual adjustable thresholds is achieved according to the similar concept of the classic industrial Ziegler-Nichols tuning method. Furthermore, all the stability analysis, reversed saturation structure, and FRMSE-based self-commissioning rule presented in this paper can be easily applied to the classic PID controller. The effectiveness and advantages of the proposed easy-implemented structures and strategies are verified by experimental results.

References

[1] K. Y. Cheng, and Y. Y. Tzou, "Fuzzy optimization techniques applied to the design of a digital PMSM servo drive," *IEEE Trans. Power Electron.*, vol. 19, no. 4, pp. 1085–1099, Jul. 2004.

[2] Y. Lai and M. Ho, "Self-commissioning technique for high bandwidth servo motor drives," in *Proc. ECCE*, 2017, pp. 342-349.

[3] C. Hsu and Y. Lai, "Novel online optimal bandwidth search and autotuning techniques for servo motor drives," *IEEE Trans. Ind. Appl.*, vol. 53, no. 4, pp. 3635-3642, Jul/Aug. 2017.

[4] Y. Chen, M. Yang, J. Long, W. Qu, D. Xu, and F. Blaabjerg, "A moderate online servo controller parameter self-tuning method via variable-period inertia identification," *IEEE Trans. Power Electron.*, vol. 34, no. 12, pp. 12165-12180, Dec. 2019.

[5] H. Butler, "Position control in lithographic equipment," *IEEE Contr. Syst. Mag.*, vol. 31, no. 5, pp. 28-47, Oct. 2011.

[6] R. M. Schmidt, G. Schitter, J. van Eij, *The Design of High Performance Mechatronics High-Tech Functionality by Multidisciplinary System Integration*. Delft: Delft University Press, 2011.

[7] K. Ogata, *Modern Control Engineering*, Englewood Cliffs, NJ: Prentice-Hall, 1970.

[8] R. Unnikrishnan, "Design of a lead compensator with minimum attenuation," *Int. J. Elect. Eng. Educ.*, vol. 17, pp. 85-88, 1980.

[9] S. Lee and W. Kim, "Active suspension control with direct-drive tubular linear brushless permanent-magnet motor," *IEEE Trans. Contr. Syst. Technol.*, vol. 18, no. 4, pp. 859-870, Jul. 2010.

[10] M. R. Issa and E. Barbieri, "Optimal PI-lead controller design," *in Proc.* SSST, 1996, pp. 364-368.

[11] X. Fu, X. Yang, P. Zanchetta, Y. Liu, C. Ding, M. Tang, and Z. Chen, "A frequency-domain data-driven adaptive iterative learning control approach: with application to wafer stage," *IEEE Trans. Ind. Electron.*, early access, 2020.

[12] Y. Li, G. Guo, and Y. Wang, "Phase lead reset control design with an application to HDD servo systems," *in Proc.* ICARCV, 2006, pp. 1-6.

[13] U. Datta, A. Kalam and J. Shi, "Battery energy storage system to stabilize transient voltage and frequency and enhance power export capability," *IEEE Trans. Power Syst.*, vol. 34, no. 3, pp. 1845-1857, May 2019.

[14] C. P. Maurya, Y. V. Hote, and V. Siddhartha, "Design of PI-lead controller for a plant having a right-half-plane zero," *in Proc. CCUBE*, 2017, pp. 1-6.

[15] K. J. Astrom and T. Hagglund, *PID Controllers: Theory, Design, and Tuning*. Research Triangle Park, NC: ISA, 1995.

[16] M. Cheng, Q. Sun, and E. Zhou, "New self-tuning fuzzy PI control of a novel doubly salient permanent-magnet motor drive," *IEEE Trans. Ind. Electron.*, vol. 53, no. 3, pp. 814-821, Jun. 2006.

[17] D. Zhang, H. Li, and E. G. Collins, "Digital anti-windup PI controllers for variable-speed motor drives using FPGA and stochastic theory," *IEEE Trans. Power Electron.*, vol. 21, no. 5, pp. 1496-1501, Sept. 2006.

[18] X. Li, J. Park, and H. Shin, "Comparison and evaluation of anti-windup PI controllers," *J. of Power Electron.*, vol. 11, no. 1, pp. 45-50, Jan. 2011.

[19] H. Shin and J. Park, "Anti-windup PID controller with integral state predictor for variable-speed motor drives," *IEEE Trans. Ind. Electron.*, vol. 59, no. 3, pp. 1509-1516, Mar. 2012.

[20] M. Yang, S. Tang and D. Xu, "Comments on "Antiwindup Strategy for PI-Type Speed Controller", " *IEEE Trans. Ind. Electron.*, vol. 62, no. 2, pp. 1329-1332, Feb. 2015.

[21] S. Yang, S. Chen, M. Chang, and J. Shyu, "Anti-windup compensation of saturated systems with phase-lead/phase-lag controller," *in Proc. 3CA*, 2010, pp. 345-348.

[22] M. Tursini, F. Parasiliti, and D. Zhang, "Real-time gain tuning of PI controllers for high-performance PMSM drives," *IEEE Trans. Ind. Appl.*, vol. 38, no. 4, pp. 1018-1026, Jul.-Aug. 2002.

[23] D. MartÃn, B. Caballero, and R. Haber, "Optimal tuning of a networked linear controller using a multi-objective genetic algorithm. Application to a complex electromechanical process," in *Proc. ICICIC*, 2008, pp. 91-91.

[24] Y. Chen, M. Yang, J. Long, K. Hu, D. Xu, and F. Blaabjerg, "Analysis of oscillation frequency deviation in elastic coupling digital drive system and robust notch filter strategy," *IEEE Trans. Ind. Electron.*, vol. 66, no. 1, pp. 90–101, Jan. 2019.

[25] I. Awaya, Y. Kato, I. Miyake, and M. Ito, "New motion control with inertia identification function using disturbance observer," in *Proc. IAS*, 1992, pp. 77-81.

[26] S. Kim, "Moment of inertia and friction torque coefficient identification in a servo drive system," *IEEE Trans. Ind. Electron.*, vol. 66, no. 1, pp. 60-70, Jan. 2019.

[27] K. Liu and Z. Zhu, "Fast determination of moment of inertia of permanent magnet synchronous machine drives for design of speed loop regulator," *IEEE Trans. Control Syst. Technol.*, vol. 25, no. 5, pp. 1816-1824, Sept. 2017.

[28] S. Villwock, and M. Pacas, "Application of the Welch-method for the identification of two- and three-mass-systems," *IEEE Trans. Ind. Electron.*, vol. 55, no. 1, pp. 457–466, Jan. 2008.

[29] Y. Chen, M. Yang, Y. Sun, J. Long, D. Xu, and F. Blaabjerg, "A modified Bi-Quad filter tuning strategy for mechanical resonance suppression in industrial servo drive systems," *IEEE Trans. Power Electron.*, to be published in 2021.

Yangyang Chen (S'19) received the B.S. degree in electrical engineering in 2016 from Harbin Institute of Technology, Harbin, China, where he is currently working toward the Ph.D. degree in power electronics and electrical drives in the School of Electrical Engineering and Automation.

His current research interests include multi-axis servo systems, mechanical resonance suppression and control parameter self-tuning strategy.

Ming Yang (M'14–SM'18) received the B.S., M.S. and Ph.D. degrees in Electrical Engineering from Harbin Institute of Technology (HIT), Harbin, China, in 2000, 2002 and 2007, respectively.

In 2004, he joined as a Lecturer with the Department of Electrical Engineering, HIT, where he has been a Professor of Electrical Engineering since 2015. From 2009 to 2012, he was a Postdoctoral Fellow with Shanghai STEP Electric Corporation. He has authored more than 80 technical papers published in journals and conference proceedings. He is the holder of more than 20 Chinese patents. His current major research interests include PMSM servo systems, predictive current control and mechanical resonance suppression.

Kaiyuan Liu received the B.S. degree in electrical engineering in 2020 from the Harbin Institute of Technology, Harbin, China. He is currently working toward the M.S. degree in power electronics and electrical drives in the School of Electrical Engineering and Automation of Harbin Institute of Technology.

His current research interests include electrical engineering and motion control.

Jiang Long received the M.S. degree in power electronics and electrical drives, in 2015, from the Harbin University of Science and Technology, Harbin, China. He is currently working towards Ph.D. degree in power electronics and electrical drives in the School of Electrical Engineering and Automation of Harbin Institute of Technology.

His current research interest focuses on PMSM servo system, predictive current control and parameter identification.

Dianguo Xu (M'97–SM'12–F'17) received the B.S. degree in control engineering from Harbin Engineering University, Harbin, China, in 1982, and the M.S. and the Ph.D. degrees in electrical engineering from Harbin Institute of Technology (HIT), Harbin, China, in 1984 and 1989 respectively.

In 1984, he joined the Department of Electrical Engineering, HIT as an Assistant Professor. Since 1994, he has been a Professor in the Department of Electrical Engineering, HIT. He was the Dean of the School of Electrical Engineering and Automation, HIT from 2000 to 2010, and the Vice President of HIT from 2014 to 2020. His research interests include renewable energy generation technology, power quality mitigation, sensorless vector-controlled motor drives, and high-performance PMSM servo system. He published over 600 technical papers.

Prof. Xu is the fellow of IEEE, the Co-EIC of IEEE TRANSACTIONS ON POWER ELECTRONICS, and the Associate Editor of IEEE TRANSACTIONS ON INDUSTRIAL ELECTRONICS. He serves as Chairman of IEEE Harbin Section.

Frede Blaabjerg (S'86–M'88–SM'97–F'03) received the Ph.D. degree in electrical engineering from Aalborg University in 1995.

He was with ABB-Scandia, Randers, Denmark, from 1987 to 1988. He became an Assistant Professor in 1992, an Associate Professor in 1996, and a Full Professor of power electronics and drives in 1998. From 2017, he became a Villum Investigator. He has published more than 600 journal papers in the fields of power electronics and its applications. He has coauthored of four monographs and editor of ten books in power electronics and its applications. His current research interests include power electronics and its applications, such as in wind turbines, PV systems, reliability, harmonics, and adjustable speed drives.

Dr. Blaabjerg has received the 31 IEEE Prize Paper Awards, the IEEE PELS Distinguished Service Award in 2009, the EPE-PEMC Council Award in 2010, the IEEE William E. Newell Power Electronics Award 2014, the Villum Kann Rasmussen Research Award 2014, and the Global Energy Prize in 2019. He was the Editor-in-Chief of the IEEE TRANSACTIONS ON POWER ELECTRONICS from 2006 to 2012. He has been the Distinguished Lecturer for the IEEE Power Electronics Society from 2005 to 2007, and the IEEE Industry Applications Society from 2010 to 2011 as well as from 2017 to 2018. From 2019 to 2020, he serves the President of IEEE Power Electronics Society. He is the Vice-President of the Danish Academy of Technical Sciences too. He is nominated in 2014–2018 by Thomson Reuters to be between the most 250 cited researchers in engineering in the world.